The initiation of frictional motion - the nucleation dynamics of frictional ruptures

Shahar Gvirtzman[1]& Jay Fineberg[1]

[1]The Racah Institute of Physics, The Hebrew University of Jerusalem, Jerusalem, Israel 91904

Key Points:

- Frictional ruptures initiate via a characteristic nucleation process that triggers dynamic rupture essentially
- Nucleation replaces the concept of a 'static friction coefficient'
- The nucleation process possesses unique characteristic general properties
- Nucleation details depend on local topography

Corresponding author: Jay Fineberg, jay@mail.huji.ac.il

Abstract

Frictional interfaces lose stability via earthquake-like ruptures, which are close analogues of shear cracks that are well-described by fracture mechanics. Interface ruptures, however, need to be first formed - or nucleated. Rupture nucleation therefore determines the onset of friction, replacing the concept of a characteristic 'static friction coefficient'. Utilizing rupture arrest at an imposed barrier, we experimentally determine nucleation locations, times and stresses at the origin of each subsequent rupture event. This enables us study the nucleation process via real-time measurements of real contact area and local strain. Nucleation events initiate as 2D patches that expand at nearly constant velocities, v_{nuc}, that are orders of magnitude lower than the dynamic rupture velocities described by conventional fracture mechanics. We find that: (1) Nucleation has location-dependent stress thresholds, (2) v_{nuc} is roughly proportional to the local stress level, (3) the nucleation process continues until the patch size reaches $L_{tran} \sim L_G$, the Griffith length for the onset of dynamic fracture (4) scaling time by $\tau = L_{tran}/v_{nuc}$, nucleation patches exhibit self-similar dynamics (5) dynamic ruptures' cohesive zones are not fully established until significantly beyond L_{tran}. Many details of nucleation are governed by the local contact area topography, which is roughly invariant under successive rupture events in mature interfaces. Topography-dependent details of the nucleation process include: precise nucleation site location, patch geometry, critical stress thresholds and the proportionality constant of v_{nuc} with stress. We believe that these results shed considerable light on both how frictional motion is triggered and earthquake initiation.

Plain Language Summary

Recent experiments have demonstrated that rapid rupture fronts, akin to earthquakes, mediate the transition to frictional motion. Moreover, once these dynamic rupture fronts ("laboratory earthquakes") are created, their singular form, dynamics and arrest are well-described by fracture mechanics. Ruptures, however, need to be created within initially rough frictional interfaces, before they are able to propagate. This is the reason that "static friction coefficients" are not well-defined; frictional ruptures can nucleate for a wide range of applied forces. A critical open question is, therefore, how the nucleation of rupture fronts actually takes place. We experimentally demonstrate that rupture front nucleation is prefaced by slow nucleation fronts. These nucleation fronts, which are self-similar, are not described by our current understanding of fracture mechanics. The nucleation fronts emerge from initially rough frictional interfaces at well-defined stress thresholds, evolve at characteristic velocity and time scales governed by stress levels, and propagate within a frictional interface to form the initial rupture from which fracture mechanics take over. These results are of fundamental importance to questions ranging from earthquake nucleation and prediction to processes governing material failure.

Introduction

The initiation of 'stick-slip' frictional motion is caused by propagating rupture fronts that detach the ensemble of discrete contacts that form a frictional interface. When occurring along a natural fault that is sandwiched between tectonic plates, this rupture process and the associated release of energy describes an earthquake (Byerlee & Brace, 1968; Scholz, 2019). These fronts have been recorded and experimentally studied over the past two decades in both brittle plastics (Rubinstein et al., 2004; Xia et al., 2004; Nielsen et al., 2010; Schubnel et al., 2011) and in rock (Wu & McLaskey, 2019; Xu et al., 2018; Passelègue et al., 2013). These rupture fronts behave precisely like shear cracks; the framework of fracture mechanics (LEFM or linear elastic fracture mechanics) fully describes rupture front characteristics, such as their propagation dynamics (Svetlizky, Kammer, et al., 2017; Passelègue et al., 2020; Kammer & McLaskey, 2019), arrest conditions (Bayart

et al., 2016, 2018), and the stress fields surrounding them (Svetlizky & Fineberg, 2014; Xu et al., 2019; Kammer & McLaskey, 2019; Mello et al., 2016).

Experiments have, moreover, demonstrated (Ben-David, Cohen, & Fineberg, 2010; Svetlizky, Kammer, et al., 2017) that a frictional system at constant nominal conditions (e.g. normal stress) will be stable to rupture for a large range of imposed initial shear stresses. Were an interface wholly homogeneous, applied stresses could be large enough to approach the maximal shear stress of a given material before the interface would 'fracture'. According to LEFM, in order for an interface to be unstable to fracture and propagate, it first requires an initial rupture or 'seed'; if no initial 'seed' exists within an interface, then the extreme (putatively singular) stress amplification that forms at a rupture tip could not take place, and ruptures would not be excited. Furthermore, this initial seed needs to surpass a critical length, called the Griffith length, L_G. LEFM predicts that a system under stress will, therefore, remain stable until an initial rupture of sufficient length is either imposed or somehow develops whose length exceeds L_G. L_G is a well-defined function of both the applied stress and system geometry; roughly speaking, the larger the imposed stress, the smaller L_G. The experimental observations of fault stability over a very wide range of initial shear stresses simply imply that a range of initial 'seed ruptures' exist; for a given 'seed' size, imposed stresses need to be sufficiently large to reduce L_G to this size. Rupture nucleation, or the formation and growth of this initial rupture within the random rough surface that characterizes a frictional interface, is, therefore, the process that *determines* when and how rupture onset will initiate in initially stressed plates.

In effect, the rupture nucleation process replaces the concept of a 'static friction' coefficient. This simple criterion for stick-slip initiation, the idea that a material characteristic 'static friction coefficient' determines whether frictional motion will occur has long been known (Rabinowicz, 1951) to be invalid. Experiments have shown that the same system can nucleate at very different initial stress levels (Ben-David, Cohen, & Fineberg, 2010; Ben-David & Fineberg, 2011; Passelègue et al., 2020). Rupture propagation, structure, and dynamics, which are all described by LEFM, are largely independent of any characteristic frictional resistance of the interface, so long as this resistance does not rapidly vary with slip velocity (Barras et al., 2020; Palmer C. & Rice R., 1973). We will demonstrate that the *local* conditions at the exact location and time of nucleation, and not a *global* 'friction law', will determine the stress at which a rupture nucleates. Once nucleation takes place, the stress distribution along the interface will then govern a rupture's eventual characteristics (Bayart et al., 2016, 2018; Ben-David, Cohen, & Fineberg, 2010; Svetlizky, Kammer, et al., 2017).

The nucleation problem is an important and open question in both the friction and fracture fields, and is crucial for the understanding of earthquakes. Below L_G, it is unclear how a small defect will grow to reach this critical length. The nucleation stage in laboratory studies of friction has been described in many studies (Ohnaka & Shen, 1999; Latour et al., 2013; Dresen et al., 2020; Popov et al., 2010; Lapusta & Rice, 2003; Uenishi & Rice, 2003; Gori et al., 2021; Hulbert et al., 2019; Leeman et al., 2018; Marone, 2019) to be slow and 'aseismic'. This is in contrast to the propagation stage, in which ruptures rapidly accelerate to high velocities and therefore emanate 'seismic' radiation. The nucleation stage is, therefore, often assumed to be qualitatively different from the dynamic rupture process. The empirical distinction between this slow process and slow rupture fronts that are described by the framework of fracture mechanics (Svetlizky, Kammer, et al., 2017; Rubinstein et al., 2007) (i.e. with crack lengths that are barely **above** the Griffith length) is rather elusive (Leeman et al., 2018). While rupture around L_G is one possible scenario for slow ruptures, it is certainly not the only possible mechanism. This important issue is still entirely open.

Several studies (Ripperger et al., 2007; Uenishi & Rice, 2003; Schär et al., 2021) have attributed the nucleation process to heterogeneity of the applied stress field. In this

view, stress heterogeneity may initiate local slip events at locations where an assumed peak strength value is surpassed. When a small slipping patch is artificially created beyond a critical length, an instability is reached and the initial patch expands spontaneously, leading to a rupture process and macroscopic sliding. This can happen with a single patch (Uenishi & Rice, 2003), or through a coalescence of several small patches(Schär et al., 2021). Other studies have proposed an avalanche-like process at the microscopic asperity level (de Geus et al., 2019), or the nucleation and propagation of excited slip pulses (Brener et al., 2018) as possible mechanisms leading to the nucleation of rapid ruptures.

Despite the importance of this process, only a relatively few detailed experimental descriptions of the nucleation process exist (Ohnaka & Shen, 1999; Latour et al., 2013; Guérin-Marthe et al., 2019; Fukuyama et al., 2018; McLaskey, 2019; Gvirtzman & Fineberg, 2021; Cebry & McLaskey, 2021; Gori et al., 2021). The reason for this lies in the very nature of the nucleation process - it is unpredictable both in space and in time, and necessitates closely following the dynamics of slip at relatively small scales. Therefore, conducting a controlled experiment that will be able to describe the process in detail is extremely challenging. For this reason, our knowledge of nucleation in the laboratory has often stemmed from examining spontaneous events that 'happen' to nucleate in a convenient location along the interface under study. While some features of this process can be understood by these means, the initial conditions at the nucleation location are generally difficult to precisely define. For example, some studies noted the significance of the rate of the nucleation process (Xu et al., 2018; Guérin-Marthe et al., 2019), but the resulting timescale could not be measured directly, since no clear starting point could be experimentally detected. As a result, in these studies the full 'nucleation time' could not be defined.

Recently, we developed a novel experimental approach that utilizes a 'remote triggering' method, which can overcome these difficulties (Gvirtzman & Fineberg, 2021). This approach enables us to conduct sequences of experiments where both the nucleation point is pre-determined and the local stress at the rupture nucleation point is measured. Precise control of the nucleation location enables us to gain a detailed description of nucleation processes by imaging the nucleation process in real time with sufficient spatial and temporal resolution. This work demonstrated that rupture nucleation is a 2D process that is not described within the current framework of fracture mechanics. The 2D spatial character of the nucleation zone has also been observed in recent experiments (Fukuyama et al., 2018; McLaskey, 2019) in rock. This work highlighted the importance of transverse rupture dynamics within the 'width' of the interface during the nucleation process. To address this issue, we utilized our optical measurement of the interface to image the *full* 2D evolution of the nucleation process. Moreover, in (Gvirtzman & Fineberg, 2021) the nucleation time was shown to depend on the local stress level, up to a threshold below which nucleation does not occur.

In this paper, we will describe the detailed characteristics of the nucleation process. In particular, we will show that all nucleation events share basic features, such as self-similar dynamics. The details of the nucleation process can significantly vary with the nucleation location, and we will demonstrate that this dependence is related to the local 'topography' at the nucleation site. Moreover, we will show the details of rupture evolution as the transition from nucleation to dynamic rupture comes about.

Experimental Apparatus

Sample construction: As in previous studies (Svetlizky & Fineberg, 2014; Ben-David, Cohen, & Fineberg, 2010; Bayart et al., 2016; Berman et al., 2020; Gvirtzman & Fineberg, 2021), we use 2 PMMA blocks to construct a frictional interface (Fig. 1). The x, y, z dimensions of the top (bottom) block are 200,100,5.5 (290,28,30)mm, respectively. The longitudinal and shear wave velocities of the blocks were ultrasonically measured (Shlomai

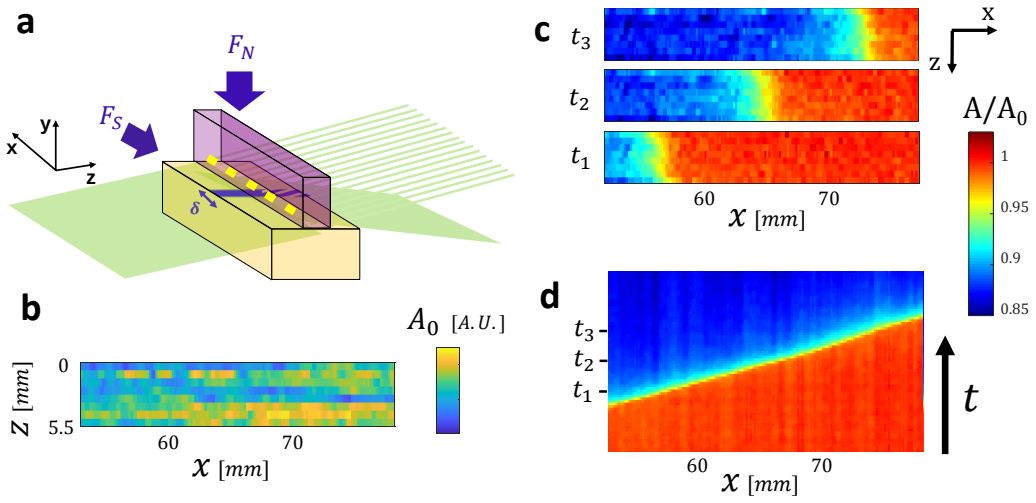

Figure 1. Experimental Setup for Nucleation Experiments. (a) A frictional interface is formed by pressing 2 PMMA blocks together with a normal force, F_N. Stick-slip behavior ensues by applying a shear load, F_S. A thick blue line marks an imposed barrier of high fracture energy at a localized position within the interface. Yellow squares denote strain gauges that are placed slightly above ($y \sim 3.5$mm) the frictional interface. The interface is illuminated by a sheet of light that is incident at an angle well beyond that of total internal reflection at a PMMA-air interface. Light transmitted through the upper block is then roughly proportional to the real area of contact, $A(x, z, t)$ at each spatial location. (b) Measurements of (the *un-normalized*) $A(x, z, t)$ of a section of the 2D interface. Colors represent the intensity of light that is transferred through each pixel. As the light intensity corresponds to the total area of the contacts within each pixel, these un-normalized measurements provide us with a map of the 'topography' of the real contact area, $A(x, z, t)$. (c) 3 snapshots of the *normalized* contact area, $A(x, z, t)/A_0(x, z)$ of the section in (b) at different times; each snapshot is normalized by its value, $A_0(x, z)$ long before rupture took place. The images are obtained at intervals $t_{(i+1)} - t_i = 20\mu s$. Sequential images throughout an experiment enable tracking of the propagating rupture front. (d) 1 dimensional representation of the interfaces are obtained by averaging over the width of the interface in the z axis. Each 2D snapshot, therefore, corresponds to a single row in the spatio-temporal picture. A rupture front is the boundary between the broken and unbroken contacts. The temporal locations of the snapshots in (c) are indicated.

et al., 2020) under plane strain conditions to obtain values of 2680 and 1361m/s, respectively, with an error of 10 m/s. These values yield a Rayleigh velocity of 1255±10m/s. The density of PMMA was measured to be $1170 \pm 10 kgm^{-3}$, and the Poisson ratio is 0.3300±0.0007. PMMA (Read et al., n.d.) is viscoelastic, with a dynamic Young's modulus of 5.75 ± 0.15GPa and a static value of 3.62 ± 0.3GPa.

Loading system: The upper block was clamped at its upper edge and was pressed to the bottom block with a normal force F_N in the y direction with a mean normal stress of 4.5 MPa (Fig 1a). F_N was held constant throughout all experiments. The bottom block was mounted on a low-friction sliding stage, which was quasistatically loaded in the $-x$ direction by applying a shear force, F_S, to produce stick-slip sequences, in which spontaneous rupture events nucleated near the x=0 edge and propagated in the x direction. Applied forces, F_N and F_S, were measured by application of these forces in series with load cells having accuracies better than 1Nt.

Real contact area measurements: We used a high-power blue LED (CBT-120) to illuminate the entire interface at an incident angle (70°) that was well beyond the total internal reflection angle (41.8°) between PMMA and air. In this way, light only passes through contact points, and therefore the intensity of transmitted light is roughly proportional to the real contact area at each point (Rubinstein et al., 2004). To visualize the entire interface, we utilized a fast camera (Phantom V710) whose 1280×8 frames were mapped to pixels of size $165 \times 688 \mu m$ in the x and z directions, respectively. The real contact area, $A(x, z, t)$, was, by this method, continuously measured at a rate of ∼580000 fps, enabling us to track the propagation of fast rupture fronts over the entire interface by visualizing the changes of $A(x, z, t)$. Rupture visualization was accomplished by normalizing each spatial point by its value, $A_0(x, z)$, long before the event started; $A(x, z, t)/A_0(x, z)$ (Fig. 1c). The non-normalized (raw) measurement, $A_0(x, z, t)$, is a map of the local distribution of contacts, or the local 'topography' (Fig. 1b). *1D* dynamics, $A(x, t)/A_0(x)$ was followed by averaging over the interface width, in the z axis (Fig. 1d). Normalization of $A(x, z, t)$ is necessary since the changes in A surrounding the rupture nucleation process are quite small (in general below $\sim 2\%$), so, without such normalization, are effectively masked by the underlying topography.

Construction of a local barrier to rupture propagation: A barrier to rupture propagation is introduced at specific locations along the interface by locally increasing the fracture energy. This is achieved by painting the interface with a permanent marker (Staedtler; size M). The (blue) marker used was transparent to the incident (blue) light used to measure $A(x, z, t)$. The marker increased (Gvirtzman & Fineberg, 2021) the local fracture energy by about a factor of 5. This was sufficient to arrest rapid spontaneously propagating ruptures that encountered it, as, locally, the energy flux to the rupture front was insufficient to overcome the increased fracture energy (Bayart et al., 2016). In the experiments presented here, we created barriers of widths 1-4 mm. After each experimental sequence, the barrier was removed by cleaning with isopropanol, and, generally, drawn at a new location. While the increase in the fracture energy due to the marker can be measured, the precise mechanism for this increase is still unknown. In general, markers are composed of minute dye particles that are chemically linked to the PMMA. They are also immersed in a solvent that dries after application. Under the huge pressures surrounding any surface contacts, it is difficult to say whether the increase in fracture energy is due to slight adhesion, due to the linker molecules, a granular (gouge-like) effect due to friction of the particles or a softening of the PMMA in a sub-micron layer below the interface resulting from the solvent.

Induced stress by rupture arrest: Ruptures, which initiated spontaneously at the sample edge ($x = 0$), immediately arrested, upon their arrival at a barrier. From their velocity immediately preceding arrest, v_{arr}, one can extract the static stress intensity factor, $K_S = K(v = 0)$, of the arrested crack as follows. We used the ruptures' equation of motion immediately prior to arrest, as described by LEFM (Freund, 1998; Svetlizky,

Kammer, et al., 2017):

$$\Gamma = G_s \cdot g(v_{arr}) = K_S^2 \cdot (1-\nu^2)/E \cdot g(v_{arr}) \tag{1}$$

where $g(v)$ is a known dynamic function (Freund, 1998), E and ν are, respectively, the dynamic Young's modulus and Poisson ratio, and G_s is the static energy release rate. It is important to note that $g(v)$ is a monotonically decreasing function of v such that $g(0) = 1$ and $1 \geq g(v) > 0$. The value of the fracture energy outside the barrier, Γ, was measured to be 1 J/m^2, for our experimental conditions (Svetlizky & Fineberg, 2014; Gvirtzman & Fineberg, 2021). Eq. 1 enabled us to determine the static stress intensity factor, K_S. The static stress intensity factor, K_S, was determined by using Eq. 1, while inputting both the measured values of Γ and v_{arr} to provide us with the value of $g(v_{arr})$. The resulting stress field ahead of the arrested crack is therefore:

$$\Delta\sigma_{xy}(v_{arr}, x) = K_S \cdot (2\pi x)^{-1/2} = \sqrt{E\Gamma/(1-\nu^2)} \cdot g(v_{arr})^{-1/2} \cdot (2\pi x)^{-1/2}. \tag{2}$$

In Eq. 2, the predicted stress field is $\Delta\sigma_{xy} = \sigma_{xy} - \sigma_{xy}^{res}$, where σ_{xy}^{res} is the residual shear stress value that remains after the passage of a rupture (Bayart et al., 2016). We define the induced stress at the nucleation point as $\sigma_{ind} = \Delta\sigma_{xy}(r^*)$, where r^* is the distance between the arrest and nucleation locations, x_{nuc}.

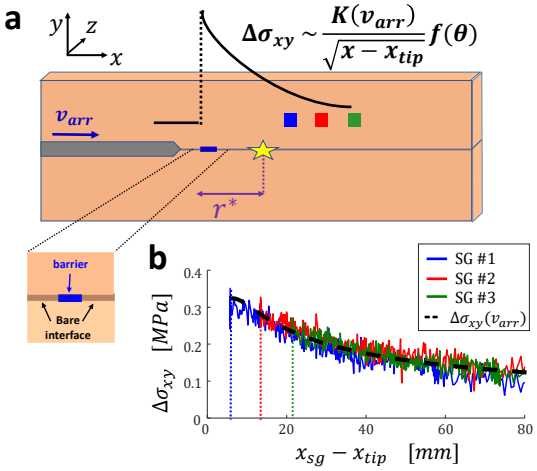

Figure 2. Validation of induced stress calculation. (a) Schematic description of the induced stress field, σ_{ind}, resulting from ruptures arrested at a barrier. The singular stress field induced by an arrested rupture, $\sigma_{ind} = \Delta\sigma_{xy}(r^*)$, was calculated using Eq. 2 using its velocity, v_{arr}, upon arrival at the barrier. This enables calculation of the stress at the nucleation point (star) located a distance r^* from the point of arrest. (b) Comparison of the calculated stress changes $\Delta\sigma_{xy}(v)$ (dashed line) induced by a moving and arrested rupture to stresses obtained via strain measurements at 3 locations, x_{sg}, along and above the interface relative to the instantaneous rupture tip locations, x_{tip} (Svetlizky & Fineberg, 2014; Freund, 1998). Vertical lines: distances between SG locations, x_{sg}, and rupture arrest point. Note that the measurements appearing beyond the vertical lines are stresses measured prior to the rupture arrest at the barrier.

While stresses could not be directly measured on the interface (the strain gages could only be mounted 3mm away from the interface), the values of the induced stresses pre-

dicted by Eq. 2 were verified by direct measurements of the stress changes, during rupture propagation and upon rupture arrest, at strain gages located, slightly above the interface, at locations $x > x_{nuc}$. Comparison of the measured σ_{xy} at the first three strain gages located beyond the barrier with the computed induced stress from the rupture tip is presented in Figs. 2a,b. The agreement between measured and computed values is excellent, and justifies our use of the computed values to obtain σ_{ind}.

Nucleation Experiments

A typical sequence of stick-slip events is shown in Fig. 3b in which a barrier was imposed at the point $x = 100$mm. In each event, spontaneous rupture fronts nucleated near the sample edge at $x = 0$ and propagated in the x direction until reaching the barrier created by the application of our marker. In the experiments considered, rupture fronts instantaneously arrested upon arrival at the barrier. This behavior is predicted by LEFM (Freund, 1998; Bayart et al., 2016) when the fracture energy of the barrier is higher than the value of the energy release rate of the incoming rupture, $G(v)$, for all values of $0 \leq v < v_{arr}$. In particular, at arrest (see Eq. 1) the static energy release rate, $G_s = \Gamma/g(v_{arr})$, is insufficient to overcome the fracture energy of the barrier, $\Gamma_{barrier}$.

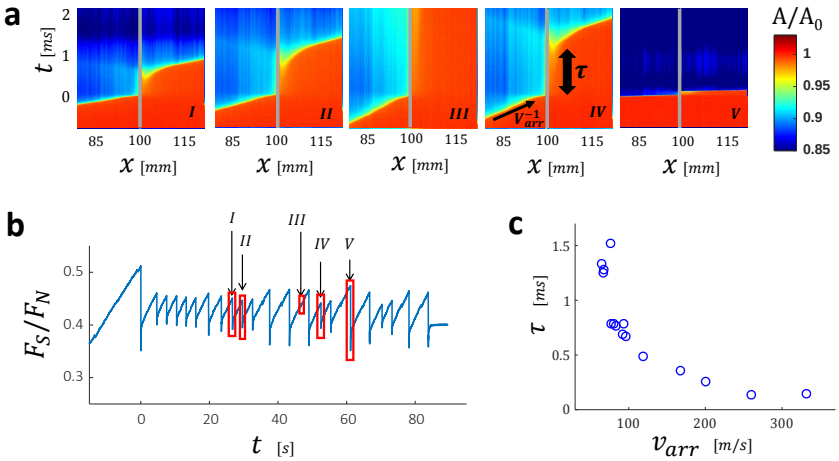

Figure 3. Nucleation Experiments. (a) Rupture arrest occurred when a rupture encountered a high fracture energy 'barrier', here imposed at location $x = 100$mm. Shown are the propagation and arrest of 5 spontaneous ruptures chosen from within a single stick-slip sequence. For events I, II, IV, and V, a nucleation event spontaneously initiated at the far side of the barrier (gray rectangle). Indicated are the velocities of the spontaneous ruptures prior to arrest, v_{arr}, and the respective timescales, τ, of the resulting nucleation process. Note that in event III, no secondary nucleation was observed. (b) The (typical) stick-slip sequence in which the events in (a) occurred. Each stress drop corresponds to a single rupture event. Noted are the events presented in (a). (c) The relation between the nucleation timescales, τ, and the velocities of the arrested crack, v_{arr}, of the full stick-slip sequence. Faster arrested cracks result in shorter nucleation processes.

Examples of rupture arrest and consequent nucleation events are presented in Fig. 3a for different values of v_{arr}. Each abrupt rupture arrest produces shear waves of sufficiently high amplitude to create a slight amount of damage as they propagated beyond the barriers and along the interface. This damage rendered them visible in the contact area measurements, as they generated $\sim 1\%$ reductions of $A(x, z, t)$ with their passage

(Gvirtzman & Fineberg, 2021). When this 'damage' is sufficiently large, these shear waves trigger the nucleation of a new rupture front near the far edge of the barrier. We believe that this damage results from the detachment of the weakest contacts in the region of high shear stress, near the barrier's far edge, created by the stress singularity of the arrested crack. A full discussion of this initial damage is found in (Gvirtzman & Fineberg, 2021). The nucleation onset is defined by the time elapsed after this shear wave passed x_{nuc}, where $x = x_{nuc}$ is the nucleation location (see Fig. 2). *This onset time is used to determine the duration, τ, of the nucleation phase.*

We define the timescale, τ, as the elapsed time between the nucleation onset and the onset of a *dynamic* rupture triggered by the nucleation process (see Fig. 3a). τ is indicative of the duration time of the nucleation process and, as shown in Fig. 3c, is a continuous, monotonically decreasing function of v_{arr}.

If nucleation occurs, it will be driven by the induced stress that is produced by the arrested rupture, $\Delta\sigma_{xy}(v_{arr}, x)$, that is described by Eq. 2. Knowledge of $\Delta\sigma_{xy}(v_{arr}, x)$ enables us to quantify the resulting stress increase at the nucleation site, $\sigma_{ind} \equiv \Delta\sigma_{xy}(v_{arr}, x_{nuc})$. In this way we are able to study the nucleation process with a known 'nucleation stress' and clear 'nucleation onset time'.

In Fig. 4a we present the dependence of τ with σ_{ind} for a typical experiment. The approximate proportionality for this event, $\tau^{-1} \propto \sigma_{ind}$, is typical (Gvirtzman & Fineberg, 2021). For each sequence of ruptures having the same nucleation point, a well defined $\sigma_{ind} = \sigma_{thresh}$ threshold exists. Below σ_{thresh}, rupture nucleation will not take place beyond the barrier (e.g. event III in Fig. 3a). The value of σ_{thresh} together with the proportionality constant relating τ^{-1} to σ_{ind} will change between different sets of experiments. Both depend on the selected location of the barrier within the interface (Gvirtzman & Fineberg, 2021). Currently, we do not know how to properly express this relation in dimensionless form.

Results

Nucleation Evolution

When a nucleation event takes place, a nucleation patch will start to slowly expand. The nucleation patch's center, x_{nuc}, is located within the damaged region created by the shear wave launched with each arrest event. As shown in the sequence of contact area measurements presented in Fig. 4b, nucleation patch expansion is a $2D$ phenomenon; the patch simultaneously expands (at about the same velocity) in both the x and z directions within the xz interface plane. When normalizing $A(x, z, t)$ to study rupture nucleation, contact area normalization was performed using $A(x, z, t_0)$, for t_0 immediately *after* the initial shear wave passage. We denote contact area measurements that are normalized in this way by $\tilde{A}(x, z)$.

As in the example presented in Fig. 4b, the edge of the nucleation patch expands via a slow and nearly constant velocity, v_{nuc}. We characterize the size of the patch, $L(t)$, by the distance from its edge to x_{nuc} along the x direction (see Fig. 4b - lower panel). In terms of $\xi(t)$, defined by (Gvirtzman & Fineberg, 2021) as the distance of the edge of the nucleation patch from the barrier edge, $L(t)+r^* = \xi(t)+\delta$, where δ is the barrier width (see Fig. 1a). Here, we choose to use the more natural quantity, $L(t)$, to describe nucleation patch extension and dynamics.

Nucleation front propagation velocities, v_{nuc}, are extremely slow. These velocities are typically 2-3 orders of magnitude lower than the velocities of the dynamic ruptures that they excite. Moreover, v_{nuc} are constant for each nucleation event. Nucleation patches do not accelerate as they propagate, in strong contrast to typical dynamic ruptures. The value of v_{nuc} is determined by σ_{ind}. Moreover, Fig 4c demonstrates that beyond loca-

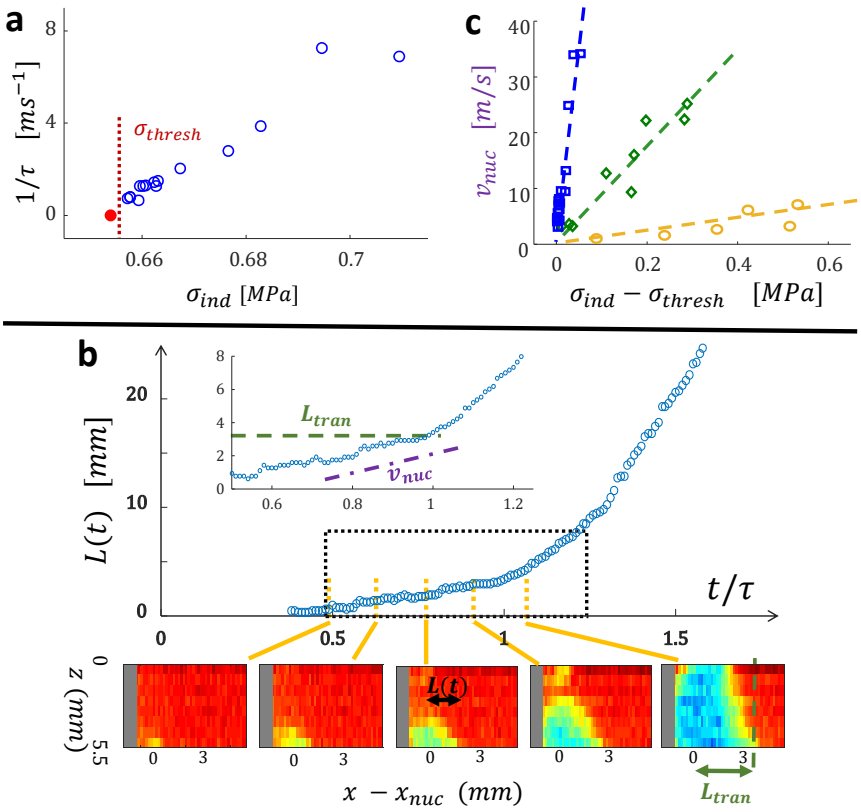

Figure 4. Slow expansion during the nucleation stage. (a) The inverse timescale of nucleation, $1/\tau$, as a function of the induced stress $\sigma_{ind} = \Delta\sigma_{xy}(r^*)$ at the nucleation point, x_{nuc} (as denoted in Fig. 2a). Open points: nucleation events from the same stick-slip sequence. The intercept with the x axis reveals a finite stress threshold, σ_{thresh}, below which nucleation does not occur (Gvirtzman & Fineberg, 2021). σ_{thresh} is determined by linearly extrapolating values of $\sigma_{ind}(v_{nuc})$ to the point where $v_{nuc} = 0$. Red point: an event where no nucleation occurred. (b) Measurements of $\tilde{A}(x, z, t)$ show how nucleation patches slowly expand in both x and z. We use $L(t)$ to characterize the $1D$ length of the nucleation patch in x. Time is normalized by τ of this event. The patch edge propagates with a slow and constant velocity, v_{nuc}, and the transition at $t = \tau$ is defined by the onset of the patch's acceleration at length $L_{tran} \equiv L(t = \tau)$. Inset: Enlargement of the region denoted by the dashed square on the main figure. Bottom: 2D snapshots of the nucleation expansion. $L(t)$ is defined as the distance from the edge of the patch to the nucleation point. (c) v_{nuc} as a function of σ_{ind} for 3 sequences of stick slip experiments. In each sequence the the barrier was placed at a different location along the interface, producing nucleation in different topographic areas. Every point corresponds to a single nucleation event and each color represents a different sequence. Each sequence is characterized by a different value of the stress threshold, σ_{thresh}. While in all sequences $v_{nuc} \propto \sigma_{ind} - \sigma_{thresh}$, suggesting a non-inertial process, the constant of proportionality as well as σ_{thresh} vary significantly with the nucleation location. Dashed lines are guides to the eye.

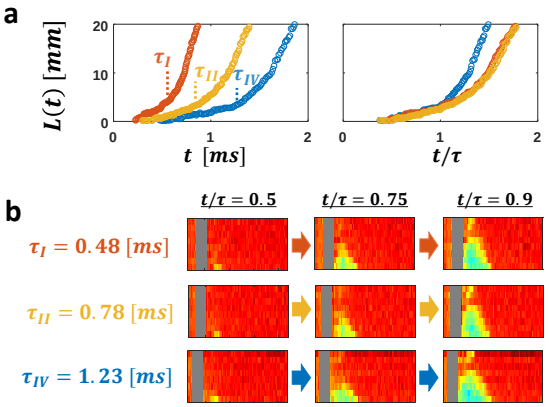

Figure 5. Self similar evolution. (a) The expansion in x, $L(t)$, of 3 different representative nucleation events from the stick-slip sequence presented in Fig. 3. Dashed lines denote the timescale, τ, of each event; indices correspond to labeled events in Fig. 3. When time is scaled by τ, all of the over 20 events in Fig. 3 collapse onto a single curve (here, only 3 are shown explicitly). Note that the collapse is valid only for $t < \tau$, during the nucleation phase. After reaching the transition point, L_{tran}, the dynamics will vary according to LEFM. (b)Snapshots of $\tilde{A}(x, z, t)$ within the nucleation region, showing the 2D self-similarity in the xz plane for the same events. When scaled by their respective values of τ, the geometric expansions of all events are nearly identical.

tion dependent thresholds, σ_{thresh}, v_{nuc} linearly depend on σ_{ind} for sets of experiments performed under varying conditions and barrier locations. Such linear behavior suggests a non-inertial process.

LEFM predicts that a rupture should be stable below the Griffith length, L_G (Freund, 1998). Moreover, beyond L_G, for the stress conditions within nucleation regions, LEFM would predict that a rupture should rapidly accelerate to nearly sonic velocities, as described by (Freund, 1998). We find that the slow and constant evolution characterized by v_{nuc} continues until $L(t)$ reaches a critical length, L_{tran} (see Fig. 4b). For $L(t) > L_{tran}$ nucleation patches accelerate sharply, exhibiting the dynamic behavior expected by LEFM. Beyond L_{tran} rupture fronts therefore enter the dynamic rupture regime (Latour et al., 2013). As demonstrated by (Svetlizky, Kammer, et al., 2017), the rapid acceleration that takes place when $t > \tau$ ($L > L_{tran}$), as well as the subsequent rupture motion, beyond possibly a short transition region, is wholly described by fracture mechanics.

We therefore identify L_{tran} with L_G. The nucleation time, τ, corresponds to the time when $L(t) = L_{tran}$. Moreover, the 3-5mm size of L_{tran} corresponds well (see Discussion section) to the calculated values of L_G for these conditions, as shown in (Gvirtzman & Fineberg, 2021).

Self Similarity of Nucleation Patches

For each sequence of rupture events, as we saw in Fig. 4a, the nucleation time, τ, is determined by the shear stress σ_{ind} at the nucleation location. Surprisingly, for each given sequence, both the nucleation patch dynamics and patch shapes are self-similar, when t is scaled by τ. A typical example is presented in Fig. 5, where 3 representative

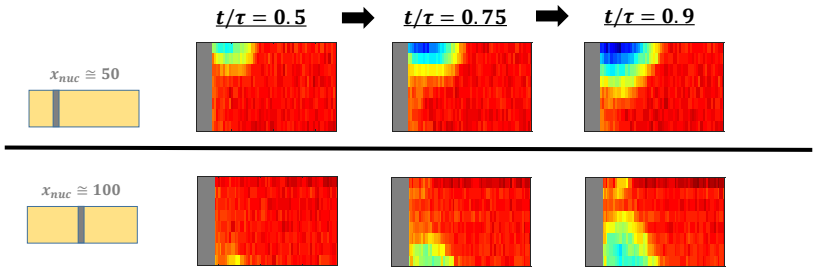

Figure 6. Different nucleation sites provide different 2D evolution. Nucleation patch dynamics at two *different* locations, x_{nuc}, selected within the interface. In both cases, the nucleation dynamics were self-similar as in Fig. 5. Each row is representative of a single sequence of events, where each column shows a snapshot of the 2D nucleation patch at a different stage of the normalized time, t/τ. The location of the barrier in each event is presented schematically at the left.

nucleation events with very different timescales, τ, are considered. Compared are the dynamics of both $L(t)$ and the entire 2D nucleation patch for these events. As a function of t/τ, the nucleation dynamics of all 3 events are nearly identical, until the dynamic rupture takes place, at L_{tran}. As values of L_{tran} are quite similar for each nucleation, we have $v_{nuc} \approx L_{tran}/\tau$.

Note that the self-similarity demonstrated in Fig. 5 takes place solely throughout the nucleation phase, before reaching the critical point at L_{tran} ($t = \tau$). Beyond this point, rupture propagation takes place according to fracture mechanics. In general, rupture evolution is quite different for different events, as seen when comparing event c in Fig. 5a, for $t > \tau$, with the other events.

Although nucleation events are self-similar, the specific *details* of their evolution depend on the local conditions at the site of nucleation. Fig. 6 demonstrates the variation of the 2D shapes and expansion rates when comparing different stick-slip sequences that nucleated at different locations within the interface. For each sequence, we chose the nucleation location by placing the barrier at different positions along the interface. Although each sequence was, itself, self-similar, the variation of the local conditions at each barrier gave rise to different nucleation patch shapes, nucleation velocities, σ_{ind} dependence and nucleation site locations relative to each barrier.

The Influence of Nucleation site Topography

$A(x,t)$, when *not* normalized, provides us with a measure of the interface 'topography', as shown in Fig. 1b. These non-normalized intensity values of the $2D$ surface measure the absolute amount of light transmitted through the interface that reflects the total area of the micro-contacts encompassed within each (x,z) pixel of our camera (Rubinstein et al., 2004). While interface topography of newly established interfaces can vary significantly with each rupture event (Morad et al., 2022), mature interfaces can stabilize their topography (Sagy et al., 2007). Indeed, throughout stick-slip sequences consisting of numerous rupture events, we find that the topography of the interface does not qualitatively change. As Fig. 7 shows, the passage of rupture fronts leaves the qualitative character of the interface topography intact. The rupture fronts, of course, do cause quantitative variations of $A(x,z,t)$, but the overall topological features (peaks, valleys, ridges) are retained by the interface. The small section described in Fig. 7 is wholly representative. Even in this single example, the different rupture events that sequentially traverse this section are wholly different in character. These events range from precursory

events, where the interface only partially ruptures (Rubinstein et al., 2007) to highly energetic events (e.g. the 4th panel in Fig. 7b) in which the overall changes in $< A >$ of this patch and the stress release (F_S/F_N) precipitated by a rupture were quite large.

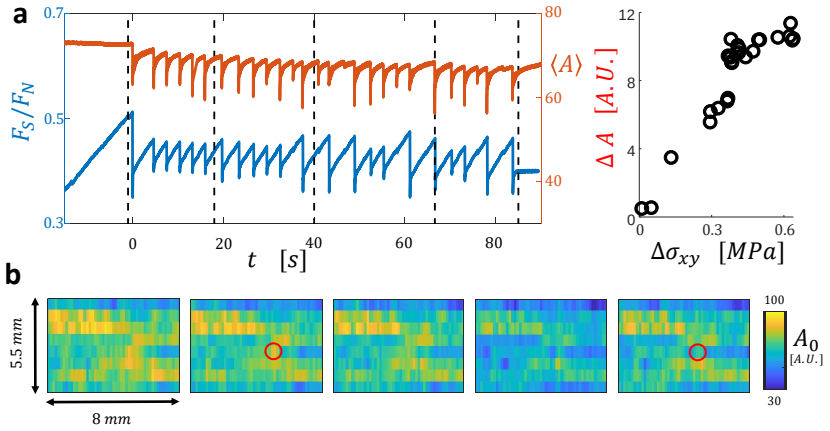

Figure 7. Overall surface topography is largely retained throughout rupture events. The overall surface topography does not change despite numerous rupture fronts that traverse the interface. Shown is the evolution of the topographical map of a nucleation region, whose dynamics are described in the lower panel of Fig. 6. The interface topography remained largely invariant throughout numerous stick-slip sequences. (a) (left) A typical stick-slip sequence consisting of 27 full and partial events. Compared are, $\langle A \rangle$, the mean values of the non-normalized contact area (red) of the typical section of the interface presented in (b) (units are arbitrary, but constant throughout the sequence) and the respective values of the applied stress ratio (blue) F_S/F_N. By both measures, the magnitudes of the different events in the sequence vary considerably. The events include system-wide as well as partial rupture (Rubinstein et al., 2007) events. (right) The corresponding contact area drops, ΔA, as a function of the peak stress drops, $\Delta\sigma_{xy}$, measured by the strain gage closest to the contact area measurements. (b) Snapshots of the non-normalized real area of contact in the section of the interface, whose mean values were quantified in (a). Colors represent the intensity of light that is transferred through each pixel, color coded from 0 to 100. The color codes describe the relative area of the asperities within each pixel that are making contact. Each pixel encompasses an area of $165 \times 688\mu m$. As single contacts are approximately $5 \times 5\mu m$, each pixel contains over 1000 contacts. Therefore, a value of 50 roughly tells us that 50% of the asperities within a given pixel are in contact relative to the areas of maximal contact (100). These statistics don't significantly depend of the value of the light threshold used. As the light intensity corresponds to the total area of the contacts within each pixel, this picture provides us the 'topography' of the real contact area, $A(x, z, t)$. The different panels correspond to the times noted by the dashed lines in (a). Despite the numerous rupture events that traversed this section, the topography has not qualitatively changed, although the overall quantitative differences are evident in $\langle A \rangle$. Some qualitative changes do occur, however, as noted by the section circled in red, which largely disappeared over the rupture sequence.

The invariance of the overall topology over long sequences of ruptures is, perhaps, surprising to one who would expect a large event to 'reset' the contact area. This observation is, however, consistent with predictions (Tabor, 1977) as well as recent exper-

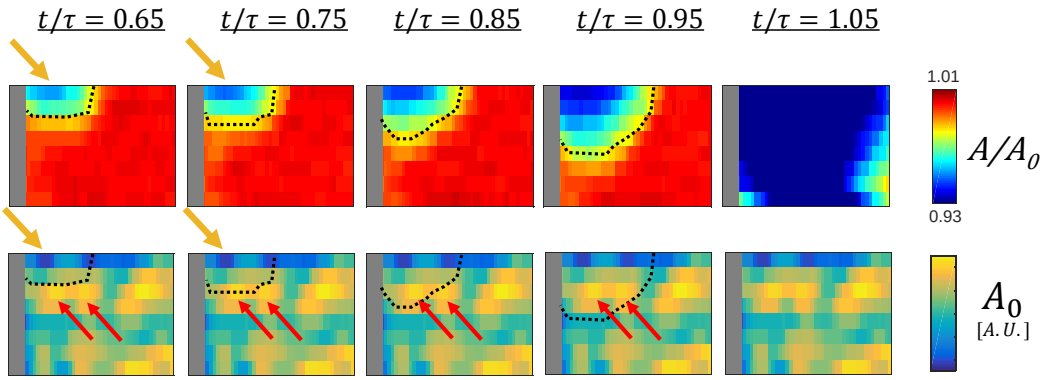

Figure 8. Local Topography guides 2D Evolution. Each column presents a snapshot during the expansion of a nucleation patch. At each stage, the top panel presents the *normalized* picture, $\tilde{A}(x,z)$, where colors corresponds to changes from the initial contact area, while the bottom panel presents the *non-normalized* intensity measurement, $A_0(x,z)$, where colors correspond to the absolute amount of contacts at this point, or the local 'toughness'. Dashed curves represent the edge of the nucleation patch on both panels. Weak (tough) points are denoted by an orange (red) arrows, respectively.

imental (Chen et al., 2020) and numerical (Pham-Ba et al., 2020) observations that suggest that the contact surface remains invariant when the slope of typical asperities becomes sufficiently small. These observations are also consistent with the numerous observations of 'repeating' earthquakes within natural faults whose seismic signatures are fairly repetitive (Sammis & Rice, 2001).

Despite the overall approximate invariance of $A(x,z,t)$, some contact area features indeed change as more and more rupture fronts traverse them. For example, in Fig. 7b, the encircled high spot connecting the two high 'ridges' in $A(x,z,t)$ was largely erased by the 27 successive ruptures that passed through the section presented. Such relatively 'small' changes in local barrier topography can precipitate very large effects, such as possibly observed in the Tohoku 2011 earthquake in which a pre-existing barrier was apparently broached (Scholz, 2014).

Let us now consider the effect of the topography of the contact area near a given barrier. The nucleation site's influence on dynamics comes to play through the local distribution of contacts - the local 'topography'. We can take advantage of our raw measurement of light passing through the interface to obtain a picture of this topography. A typical example of how topography influences nucleation front dynamics is presented in Fig. 8. In the figure we compare the topographical map of the nucleation area to the path selected by a nucleation front at different moments in time, in the region of the barrier imposed at 50mm (the event described in the upper panels of Fig. 6). Here we follow the evolution of a nucleation patch in the normalized and non-normalized representations of the contact area where, in the latter, we sketch the nucleation patch boundaries at each instant. There are two factors that influence the selection of the nucleation point. (1) The proximity to the barrier is important; the closer to the barrier, the higher the magnitude of the induced stress field, σ_{ind}, generated by the arrested crack location (see Fig. 2a). (2) An additional key factor for selection of the nucleation location is the local topography; the lower the contact area (weaker the location) the easier it will be to initiate rupture. We see the influence of both of these factors in the example presented

in Fig. 8. The initiation of the patch (denoted by an orange arrow) is, indeed, located at one of the weakest points in the near vicinity of the barrier.

Once nucleation takes place, we find that the local topography will serve to guide the path and geometry of the nucleation front. As Fig. 8 demonstrates, local 'tough' points - hotter colors - indeed influence the nucleation evolution. A ridge of tough points (red arrows) seems to both guide the nucleation front and 'delay' its 2D expansion. These rather small heterogeneities have a large impact on the dynamics of the very slow nucleation fronts; after overcoming the tough points, patches will often 'jump'. On the other hand, local toughness variations along the interface will generally not influence the propagation of a fast crack. At the onset of propagation, we expect that the *physical* heterogeneity of the surface itself will have a much larger influence on guiding a crack front than, for example, the heterogeneity of the stress field (Ripperger et al., 2007). The reason for this expectation is that the fracture energy (contact strength) is a local quantity. At each location, a rupture front must 'compare' the energy flux into its tip (an integral quantity) with the fracture energy, a local one. Whereas local strengths can fluctuate widely, as the map in Fig. 8 suggests, the energy flux is determined by the mean values of the surrounding fields. The energy flux is, therefore, a smooth function of the position and is not heavily influenced by small-scale fluctuations of the stress field.

We also find that, once the nucleation front expands over the entire span of the interface, its dynamics are significantly affected (Fukuyama et al., 2018; McLaskey, 2019; Gvirtzman & Fineberg, 2021), and it will generally increase its propagation speed.

The buildup of the cohesive zone

As the nucleation patch expands beyond the critical point, L_{tran}, it undergoes a rapid acceleration and propagates rapidly according to fracture mechanics (Svetlizky, Kammer, et al., 2017). Cracks are, in LEFM, considered to be singular objects whose tip is described by putatively singular stress fields, $\sigma_{i,j} \propto K/r^{1/2}$. Nature, however, will not countenance mathematically singular fields and real cracks are more complex objects. In particular, the singular fields at their tips must be regularized or 'blunted'. The region in which rupture-tip singularities are blunted is generally called a 'cohesive zone' (Freund, 1998; K. Bertram Broberg, 1999). This region bridges the gap between the (approximately constant) shear stresses along the interfaces at the tail of a rupture and the approximate singularity at its tip, and essentially describes the region in which the fracture process is taking place at the rupture tip. Only recently (Svetlizky & Fineberg, 2014; Berman et al., 2020) has this rather elusive region been experimentally observed for a dynamic rupture, in cases of 'fully developed' frictional ruptures.

The cohesive zone, however, needs to be formed by a crack. In fully developed cracks, the form and scale of this region are dependent on the propagation velocity (Freund, 1998; K. Bertram Broberg, 1999), but for frictional cracks (for the conditions in these experiments) the extent of the cohesive zone of relatively slow cracks has been shown to extend over a few mm (Svetlizky & Fineberg, 2014; Berman et al., 2020) in the vicinity of the rupture tip. At $t = \tau$, the size of the nucleation patch is at this scale. The cohesive zone, however, is not necessarily fully developed.

We now are in a position to study how the cohesive zone development takes place, by monitoring the development of $A(x,t)$ for $t > \tau$. Prior studies have shown (Svetlizky & Fineberg, 2014) that the near-tip shape of $A(x,t)$ is a way to experimentally characterize the cohesive zone, as this is precisely the region in which a propagating rupture transforms the initially intact interface ($\tilde{A} = 1$) to one in which the contact area is both reduced and conceivably weakened. This region is where contact 'fracture' is taking place. The reduction of A at a rupture tip is a weak function of the propagation velocity (Svetlizky, Bayart, et al., 2017). For the slowest rupture velocities, (Svetlizky, Bayart, et al., 2017) found that $\tilde{A} \approx 0.9$ behind the rupture tip, yielding $\Delta A \equiv (A - A_{res})/A_0 > 0.1$,

where A_{res} is the residual contact area of a fully developed rupture front. Rupture propagation velocity, moreover, influences more than simply the magnitude of the drop in the contact area. For example, recent studies of frictional ruptures (Berman et al., 2020) in these materials have revealed that the cohesive zone structure, in fact, also changes dramatically with the propagation velocity.

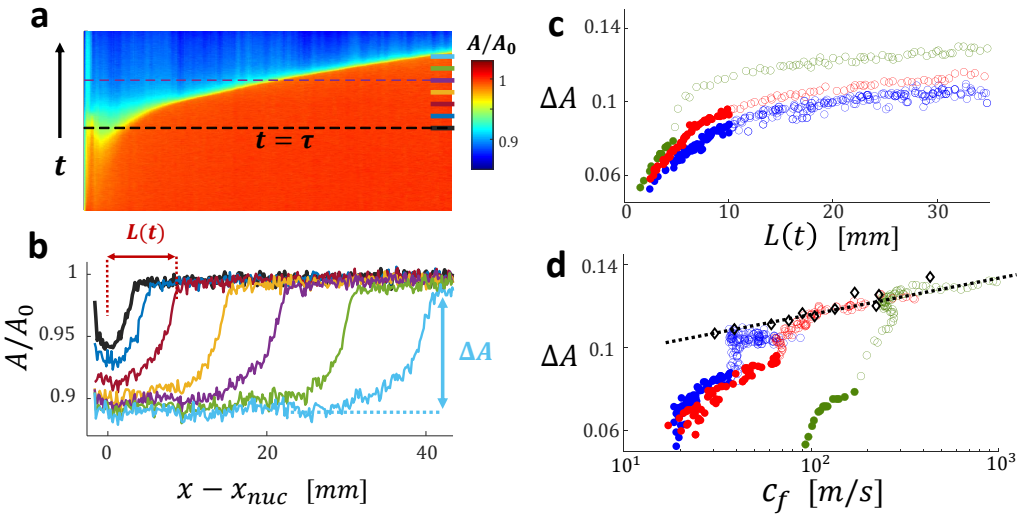

Figure 9. Cohesive zone growth: from nucleation to propagation. (a) Spatio-temporal picture of the evolution in x (integrated over z) of $A(x,t)/A_0$ throughout the transition from the nucleation stage to dynamic rupture. (b) Profiles of the 1D normalized contact area, $\tilde{A}(x - x_{nuc})$, from the data presented in (a) for $t \geq \tau$. The time of each profile is denoted by the bars on the right edge of (a); plot colors correspond to respective bar colors. The profile at $t = \tau$ is marked in black. Rupture lengths, $L(t)$, are defined with respect to x_{nuc}, and ΔA is defined as the maximum drop in contact area within the tail of the rupture front. (c) ΔA as a function of $L(t)$, for 3 different events from the same stick-slip sequence, where $t \geq \tau$. Red symbols correspond to the event presented in (a,b). (d) ΔA as a function of rupture front velocities, $c_f = \dot{L}$, in a semilog representation. Black symbols denote the contact area drop of all spontaneous *fully developed* rupture fronts belonging to this sequence, prior to their arrest at the barrier. The dashed line is a guide for the eye. The logarithmic dependence of the values of $\Delta A(c_f)$ was previously described in (Svetlizky, Bayart, et al., 2017). Full circles in (c-d) denote the propagation stage prior to the final jump to fully developed values of ΔA.

In Fig. 9 we present the evolution of ΔA as a function of the distance, $x - x_{nuc}$, at times beyond $t = \tau$. Fig. 9 demonstrates that at the onset of dynamic rupture $\Delta A \approx 0.05$, and has not yet reached its fully developed value. As the rupture progresses and accelerates, ΔA increases until, only at $x - x_{nuc} \sim 20mm$ does ΔA attain the value compatible with a fully developed rupture front. It is interesting that the growth of ΔA is not 'continuous'. For each of the 3 examples described in Figs. 9c,d, ΔA undergoes a nearly discontinuous 'jump' to its steady-state value as seen in Fig. 9d; after τ, ΔA grows continuously from ≈ 0.05 to $\Delta A \approx 0.075 - 0.09$ before making a rapid 'jump' to its fully developed value. The ΔA values for a fully developed ruptures were determined from the rupture fronts prior to their arrest at the barriers (black symbols in Fig. 9d), which correspond to the measurements of (Svetlizky, Bayart, et al., 2017). In summary, we find that the full development of the cohesive zone does not take place within

the nucleation stage. During the slow evolution of the nucleation patch ΔA grows to a value of $\sim$ 0.05. After the transition at $t = \tau$, ΔA continues to develop until reaching its velocity dependent value for a fully developed rupture front.

Discussion

Here, we have focused on characterizing the nucleation process, which, in contrast to dynamic rupture, is not a process that is described in our current understanding of fracture mechanics. To achieve this, we have utilized our knowledge of fracture mechanics to establish well-defined conditions that enable a detailed study of rupture nucleation; we used 'artificially' arrested ruptures to provide quantitative characterizations of both the location and conditions for which nucleation takes place.

This technique for generating nucleation events can, essentially, be considered a demonstration of 'remote triggering' of earthquakes.

As shown in (Gvirtzman & Fineberg, 2021), arrested ruptures generate a wave propagating at approximately the shear wave speed, C_S, that slightly reduces $A(x, z, t)$ along its path. This slight damage creates a well-defined starting point in time for nucleation. We surmise that these processes are similar to remote triggering processes that are sometimes observed upon the arrest of large natural earthquakes (Brodsky & van der Elst, 2014). This mechanism may also be involved in the excitation of aftershocks in the close vicinity of an arrested earthquake.

Despite this 'dynamic' triggering of nucleation, we believe that the ensuing nucleation dynamics are actually quite general. As shown in Fig. 4b, stresses at the nucleation site must surpass a location-dependent threshold value. In the work described here, we have 'artificially' created these conditions, where the high stress induced by an arrested rupture on one side of the barrier generated a high-stress region beyond the barrier's other side.

By this method, we have demonstrated that the process of nucleation is a well-defined continuum process whose dynamics are qualitatively similar at each barrier location. In particular:

- The nucleation process is the vehicle that will create an initial rupture – bringing the initial nucleation patch to a size (corresponding to the Griffith length) at which a frictional system loses stability to dynamic fracture.
- All nucleation patches observed have a distinct 2D character. Nucleation fronts are well-defined entities that propagate at velocities, v_{nuc} that are 2-3 orders of magnitude below typical rupture velocities. The values of v_{nuc} are determined by the shear stress values, σ_{ind}, surrounding the nucleation location. Below a threshold value for σ_{ind} nucleation can not take place.
- For nucleation to occur, we require a combination of a high stress concentration and a locally weak region.
- While nucleation is a continuum process, heterogeneity along an interface (of either stresses, local values of the fracture energy, or even prior rupture history) will be a deciding factor in where, when and in what form nucleation will take place.Thus, local topography highly influences the details of the progression of nucleation patches (Fryer, B., Giorgetti, C., Passelègue et al., 2022).
- Self-similar evolution of nucleation patches will only be evident so long as the important topographical features at nucleation site remains invariant. We have shown that, in the 'mature faults' described in these experiments, the interface topography indeed remains approximately invariant - despite numerous rupture fronts that traverse a given area.

Relation to previous work

The nucleation process described here is, essentially, a quantitative extension of Ohnaka's description (Ohnaka & Shen, 1999) of rupture nucleation. One difference is, perhaps, that we have clearly shown that there are two distinctly different processes that describe frictional ruptures; a distinct nucleation phase that couples to the phase of rapid rupture that is described by fracture mechanics. These observations complement and expand the observations of Latour (Latour et al., 2013) , Gori et al (Gori et al., 2021), and McLaskey (McLaskey, 2019; Cebry & McLaskey, 2021).

Rupture nucleation, of course, can also be initiated by means other than those used here, for example by fluid injection. Fluid injection both locally decreases the normal pressure, thereby weakening the interface, as well as increases the background shear stress, as in our experiments. The effects of nucleation via fluid injection can be seen in the enhanced seismic activity in locations where hydrofracture is implemented (Schultz et al., 2020). Nucleation by fluid injection has also been studied in recent experiments (Cebry & McLaskey, 2021; Gori et al., 2021) whose qualitative observations were, in many respects, very similar to the nucleation process demonstrated here. Fluid injection created slow nucleation patches that expanded well beyond the region that the injected fluid could reach, suggesting that the stresses created by the injection process dominate the expansion. Slow patch expansion took place until patches reached lengths (we surmise the Griffith length) where rapid dynamic ruptures were triggered. From this point, ruptures accelerated and propagated at dynamic velocities.

The retention of local topography

The retention of the local topography in our experiments (e.g. Fig. 7) may appear rather surprising; one could expect that significant sliding along the interface that takes place in multiple successive events should crush or at least largely modify any significant topological features. Such topography retention will certainly not *always* take place. Recent experiments (Morad et al., 2022) have indeed demonstrated that 'new' interfaces, created by the controlled fracture of intact rock, evolve dramatically with slip. We might understand these apparent disparities in light of recent work (Pham-Ba et al., 2020) that has demonstrated the validity of the 'Tabor parameter' (Tabor, 1977) as a condition for contact rupture. Above a critical roughness, asperities will fracture and surfaces will be ground down. Below this value faults are 'mature', plastic deformation of asperities is expected for which interface topography will be fairly well conserved. This situation had been previously noticed in early simulations (Ben-Zion & Rice, 1995) where repeatability of earthquakes was seen to be related to grid-size dependence. Further support for this condition has also been recently observed in rock friction (Chen et al., 2020). The retention of interface topography should be a necessary condition for the numerous instances of repeating earthquakes that are routinely observed within natural faults (Sammis & Rice, 2001; Uchida & Bürgmann, 2019).

Rupture beyond nucleation

The strong dependence of the details of the nucleation process on the local topography is, we believe, due to the fact that nucleation is a threshold process; any perturbation of the conditions around the requisite threshold will have a strong influence. Once, however, the transition to dynamic fracture occurs, the influence of topography will lessen considerably.

In dynamic fracture the ensemble dynamics do not react to individual asperities, but instead relate to a continuous mean (and mesoscopic) quantity that characterizes the fracture surface, the fracture energy. That said, sufficiently large heterogeneity at

large scales will influence fracture dynamics – this property was utilized here to cause the rupture arrests that triggered the subsequent nucleation process.

We would like to add a few words regarding interface rupture as described by dynamic fracture. When a frictional rupture propagates, it leaves in its wake a residual stress residual shear stress at each point, $\sigma_{xy}^{res}(x)$. So long as σ_{xy}^{res} is not a strong function of the slip velocity (Roch et al., 2022; Barras et al., 2019, 2020), the description of rupture can be perfectly mapped to the fracture mechanical description for shear fracture (Palmer C. & Rice R., 1973). The stability of an initial 'interface crack' is determined by the instantaneous balance of energy; the global amount elastic energy within the *entire* system (above the shear stress level determined by σ_{xy}^{res}) is balanced by the local dissipation at the interface defined by the fracture energy. There is no 'threshold value' for the imposed elastic energy in a system. The greater the imposed shear stress beyond σ_{xy}^{res} prior to nucleation (or, equivalently, the larger the amount of existent elastic energy prior to rupture nucleation) the larger a rupture's acceleration towards either the Rayleigh wave speed or beyond (Kammer & McLaskey, 2019; Passelègue et al., 2020), once nucleation takes place. Moreover, all of consequent rupture dynamics are described (Svetlizky, Kammer, et al., 2017; Kammer et al., 2018) by fracture mechanics. This picture has been validated by numerous experiments over the past decade (Ben-David, Cohen, & Fineberg, 2010; Ben-David & Fineberg, 2011; Svetlizky, Kammer, et al., 2017; Passelègue et al., 2013; Wu & McLaskey, 2019; Xu et al., 2019; Passelègue et al., 2020; Rubino et al., 2017; Yamashita et al., 2018; Chen et al., 2021).

In general, this balance of energy enables dynamic ruptures to possess an energy 'buffer' that they can draw on to overcome local barriers. This energy buffer comes at the expense of their propagation velocity. Depending on a rupture's instantaneous propagation speed, the rupture can, to a point, increase the energy flux at its tip by slowing down, if required to overcome a fracture energy barrier. As ruptures approach C_R, this dynamic energy buffer becomes huge. As $C_f \rightarrow C_R$, even the large barriers created here are easily overcome.

This entire description of rupture dynamics is, however, contingent on an important condition; *that an initial crack is in existence.* Without an initial flaw (or crack) the singular focusing of energy to the rupture tip that enables the LEFM description can not take place. The fracture mechanics framework can not describe how this initial rupture is created. This framework can only describe its stability and ensuing dynamics assuming that it exists. For this reason, the nucleation process is critical as, without it, an interface will always be stable to fracture - no matter what the level of initially imposed energy in the system.

In a sense, rupture nucleation is analogous to the conditions leading to a forest fire. Forest conditions must be sufficiently dry - the drier the forest the larger the potential for a large conflagration. Whether a forest fire will initiate or not at a given time, however, depends on whether someone 'lights a match' (nucleation).

The relation between L_{tran} and the Griffith length

In the section entitled 'Nucleation Evolution' (Fig. 4 and 5) we demonstrated that nucleation patch growth is the vehicle that brings a frictional system a well-defined transition length, L_{tran} after rapid rupture dynamics initiate. How does L_{tran} compare to the Griffith length, L_G, the relevant scale for the nucleation of dynamic fracture? Gvirtzman et al. (Gvirtzman & Fineberg, 2021) calculated L_G, via energy balance, for the geometric and stress conditions in these experiments. These calculations yielded values of $3-5mm$, in good agreement with our measurements of L_{tran}. The close agreement between L_{tran} and L_G indeed supports the idea that the nucleation process is indeed the vehicle that brings the system to LEFM-described dynamics. (The nucleation process in essence *replaces* the concept of a critical static friction coefficient).

In the literature there are two other, quite different, criteria for the stability of a frictional interface. Below, we demonstrate that each of these criteria predict values for L_{tran} that are much larger than the measured values.

Let us first consider the calculated stability of a frictional interface separating two rigidly sliding bodies that are coupled by the friction law described by Rate and State friction. This calculation (Rice et al., 2001) yielded a critical nucleation length, at which the steady slide becomes unstable to be:

$$L_c^{R/S} = \mu D_c \pi / [(b-a) \cdot \sigma_0] \tag{3}$$

In our experiments, the shear modulus and normal load are, respectively, $\mu = 2GPa$ and $\sigma_0 = 4.5MPa$. The slip distance $D_c \approx 5\mu m$ was obtained from direct measurements of the cohesive zone size (Berman et al., 2020). Values of the coefficients $a \approx 0.008$ and $b \approx 0.015$ for PMMA under our experimental conditions were measured separately (Ben-David, Rubinstein, & Fineberg, 2010; Baumberger & Caroli, 2006). Applying these values to Eq. 3 yields $L_c^{R/S} \approx 1m$, which is 2-3 orders of magnitude larger than the measured value of L_{tran}.

Let us now consider the critical length for instability suggested by Uenishi and Rice (Uenishi & Rice, 2003; de Geus et al., 2019; Schär et al., 2021), which assumes a slip weakening friction law in the vicinity of a near-critical value of shear stress. Here, the estimated critical length was predicted to be:

$$L_c^{UR} = 1.158 \mu D_c / [\sigma_{peak} - \sigma_{res}] \tag{4}$$

where σ_{peak} and σ_{res} are, respectively, the peak and residual stress values of a frictional interface. These can be related to the fracture energy, Γ, by means of the slip weakening definition of $\Gamma = \frac{1}{2} \cdot D_c \cdot [\sigma_{peak} - \sigma_{res}]$. Inputting the measured value of $\Gamma = 1 J/m^2$ (Svetlizky & Fineberg, 2014; Gvirtzman & Fineberg, 2021) and $D_c \sim 5\mu m$ (as above) into Eq.4 yields a value of $L_c^{UR} \approx 3cm$, which is about an order of magnitude larger than L_{tran}.

What is ahead

What are we still missing? Our fundamental understanding of rupture nucleation processes within frictional interfaces and earthquake dynamics is very much in its infancy. In this work, we have provided a first step, the empirical characterization of this critical process. In particular, we have presented evidence that nucleation is not clearly related to the standard fracture mechanics framework; nucleation is stress driven, occurs below L_G, and is characterized by propagation velocities that are considerably below typical rupture speeds. We currently lack a theoretical understanding and description of this important process. At present, we do not even possess the requisite insight to properly non-dimensionalize expressions such as $v_{nuc} \propto \sigma_{ind}$. We believe that a theoretical description of these processes should also be able to properly relate the mesoscopic scales (e.g. nucleation patch size and shape) to the microscopic topographical features of the interface in the nucleation region. These goals still remain as significant theoretical challenges.

Acknowledgments

Both JF and SG acknowledge the support of the Israel Science Foundation grant 840/19. We also wish to acknowledge the invaluable advice and comments provided by M. Adda-Bedia.

Data Availability

All data used in this work is publicly available on 4TU Centre for Research Data. Dataset: https://doi.org/10.4121/21523512.v2.

References

Barras, F., Aldam, M., Roch, T., Brener, E. A., Bouchbinder, E., & Molinari, J.-F. (2019, NOV 26). Emergence of cracklike behavior of frictional rupture: The origin of stress drops. *PHYSICAL REVIEW X*, *9*(4). doi: 10.1103/PhysRevX.9.041043

Barras, F., Aldam, M., Roch, T., Brener, E. A., Bouchbinder, E., & Molinari, J. F. (2020, feb). The emergence of crack-like behavior of frictional rupture: Edge singularity and energy balance. *EARTH AND PLANETARY SCIENCE LETTERS*, *531*. doi: 10.1016/j.epsl.2019.115978

Baumberger, T., & Caroli, C. (2006). Solid friction from stick–slip down to pinning and aging. *Advances in Physics*, *55*(3-4), 279-348. Retrieved from `https://doi.org/10.1080/00018730600732186` doi: 10.1080/00018730600732186

Bayart, E., Svetlizky, I., & Fineberg, J. (2016). Fracture mechanics determine the lengths of interface ruptures that mediate frictional motion. *Nature Physics*. doi: 10.1038/nphys3539

Bayart, E., Svetlizky, I., & Fineberg, J. (2018, may). Rupture Dynamics of Heterogeneous Frictional Interfaces. *Journal of Geophysical Research: Solid Earth*, *123*(5), 3828–3848. doi: 10.1002/2018JB015509

Ben-David, O., Cohen, G., & Fineberg, J. (2010, oct). The Dynamics of the Onset of Frictional Slip. *Science*, *330*(6001), 211–214. Retrieved from `https://www.sciencemag.org/lookup/doi/10.1126/science.1194777` doi: 10.1126/science.1194777

Ben-David, O., & Fineberg, J. (2011). Static friction coefficient is not a material constant. *Physical Review Letters*. doi: 10.1103/PhysRevLett.106.254301

Ben-David, O., Rubinstein, S. M., & Fineberg, J. (2010). Slip-stick and the evolution of frictional strength. *Nature*, *463*(7277). doi: 10.1038/nature08676

Ben-Zion, Y., & Rice, J. R. (1995). Slip Patterns and Earthquake Populations Along Different Classes of Faults in Elastic Solids. *Journal of Geophysical Research-Solid Earth*, *100*(B7), 12959–12983.

Berman, N., Cohen, G., & Fineberg, J. (2020, sep). Dynamics and properties of the cohesive zone in rapid fracture and friction. *Physical Review Letters*, *125*(12). doi: 10.1103/PHYSREVLETT.125.125503

Brener, E. A., Aldam, M., Barras, F., Molinari, J. F., & Bouchbinder, E. (2018, dec). Unstable slip pulses and earthquake nucleation as a nonequilibrium first-order phase transition. *Phys. Rev. Lett.*, *121*(23), 234302. doi: 10.1103/physrevlett.121.234302

Brodsky, E. E., & van der Elst, N. J. (2014). The Uses of Dynamic Earthquake Triggering. *Annual Review of Earth and Planetary Sciences*, *42*(1), 317–339. Retrieved from `https://doi.org/10.1146/annurev-earth-060313-054648` doi: 10.1146/annurev-earth-060313-054648

Byerlee, J. D., & Brace, W. F. (1968). Stick Slip, Stable Sliding, and Earthquakes-Effect of Rock Type, Pressure, Strain Rate, and Stiffness. *JOURNAL OF GEOPHYSICAL RESEARCH*, *73*(18). doi: 10.1029/JB073i018p06031

Cebry, S. B. L., & McLaskey, G. C. (2021). Seismic swarms produced by rapid fluid injection into a low permeability laboratory fault. *Earth and Planetary Science Letters*, *557*, 116726. Retrieved from `https://www.sciencedirect.com/science/article/pii/S0012821X20306701` doi: https://doi.org/10.1016/j.epsl.2020.116726

Chen, X., Carpenter, B. M., & Reches, Z. (2020, jul). Asperity Failure Control

of Stick-Slip Along Brittle Faults. *PURE AND APPLIED GEOPHYSICS*, *177*(7), 3225–3242. doi: 10.1007/s00024-020-02434-y

Chen, X., Chitta, S. S., Zu, X., & Reches, Z. (2021). Dynamic fault weakening during earthquakes: Rupture or friction? *Earth and Planetary Science Letters*, *575*, 117165. Retrieved from `https://www.sciencedirect.com/science/article/pii/S0012821X21004209` doi: https://doi.org/10.1016/j.epsl.2021.117165

de Geus, T. W. J., Popović, M., Ji, W., Rosso, A., & Wyart, M. (2019, nov). How collective asperity detachments nucleate slip at frictional interfaces. *Proceedings of the National Academy of Sciences of the United States of America*, *116*(48), 23977–23983. Retrieved from `https://github.com/tdegeus/GooseFEMandhttps://github.com/tdegeus/ElastoPlasticQPot` doi: 10.1073/PNAS.1906551116/SUPPL_FILE/PNAS.1906551116.SAPP.PDF

Dresen, G., Kwiatek, G., Goebel, T., & Ben-Zion, Y. (2020, dec). Seismic and Aseismic Preparatory Processes Before Large Stick–Slip Failure. *Pure and Applied Geophysics*, *177*(12), 5741–5760. Retrieved from `https://link.springer.com/article/10.1007/s00024-020-02605-x` doi: 10.1007/S00024-020-02605-X/FIGURES/8

Freund, L. (1998). *Dynamic fracture mechanics*. Retrieved from `https://books.google.com/books?hl=en&lr=&id=B2sophpCOIYC&oi=fnd&pg=PR11&ots=CuULPl3TEM&sig=LW_y8bh7CuB5xi5bqOAWnJjX9dA`

Fryer, B., Giorgetti, C., Passelègue, F., Momeni, S., Lecampion, B., . V., & M. (2022). The Influence of Roughness on Experimental Fault Mechanical Behavior and Associated Microseismicity. *Journal of Geophysical Research: Solid Earth*, *127*.

Fukuyama, E., Tsuchida, K., Kawakata, H., Yamashita, F., Mizoguchi, K., & Xu, S. (2018). Spatiotemporal complexity of 2-D rupture nucleation process observed by direct monitoring during large-scale biaxial rock friction experiments. *Tectonophysics*. doi: 10.1016/j.tecto.2017.12.023

Gori, M., Rubino, V., Rosakis, A. J., & Lapusta, N. (2021, dec). Dynamic rupture initiation and propagation in a fluid-injection laboratory setup with diagnostics across multiple temporal scales. *Proceedings of the National Academy of Sciences of the United States of America*, *118*(51). doi: 10.1073/PNAS.2023433118/-/DCSUPPLEMENTAL

Guérin-Marthe, S., Nielsen, S., Bird, R., Giani, S., & Di Toro, G. (2019, jan). Earthquake Nucleation Size: Evidence of Loading Rate Dependence in Laboratory Faults. *Journal of Geophysical Research: Solid Earth*, *124*(1), 689–708. doi: 10.1029/2018JB016803

Gvirtzman, S., & Fineberg, J. (2021, aug). Nucleation fronts ignite the interface rupture that initiates frictional motion. *Nature Physics 2021 17:9*, *17*(9), 1037–1042. Retrieved from `https://www.nature.com/articles/s41567-021-01299-9` doi: 10.1038/s41567-021-01299-9

Hulbert, C., Rouet-Leduc, B., Johnson, P. A., Ren, C. X., Rivière, J., Bolton, D. C., & Marone, C. (2019). Similarity of fast and slow earthquakes illuminated by machine learning. *Nature Geoscience*. doi: 10.1038/s41561-018-0272-8

K. Bertram Broberg. (1999). *Cracks and Fracture*. Academic Press, London.

Kammer, D. S., & McLaskey, G. C. (2019). Fracture energy estimates from large-scale laboratory earthquakes. *Earth and Planetary Science Letters*, *511*. doi: 10.1016/j.epsl.2019.01.031

Kammer, D. S., Svetlizky, I., Cohen, G., & Fineberg, J. (2018). The equation of motion for supershear frictional rupture fronts. *Science Advances*, *4*(7), eaat5622. Retrieved from `https://www.science.org/doi/abs/10.1126/sciadv.aat5622` doi: 10.1126/sciadv.aat5622

Lapusta, N., & Rice, J. R. (2003, apr). Nucleation and early seismic propagation of small and large events in a crustal earthquake model. *Journal of Geophysical*

Research: Solid Earth, *108*(B4). doi: 10.1029/2001JB000793

Latour, S., Schubnel, A., Nielsen, S., Madariaga, R., & Vinciguerra, S. (2013). Characterization of nucleation during laboratory earthquakes. *Geophysical Research Letters*. Retrieved from https://agupubs.onlinelibrary.wiley.com/doi/full/10.1002/grl.50974 doi: 10.1002/grl.50974

Leeman, J. R., Marone, C., & Saffer, D. M. (2018, sep). Frictional Mechanics of Slow Earthquakes. *JOURNAL OF GEOPHYSICAL RESEARCH-SOLID EARTH*, *123*(9), 7931–7949. doi: 10.1029/2018JB015768

Marone, C. (2019). The spectrum of fault slip modes from elastodynamic rupture to slow earthquakes. In Bizzarri, A and Das, S and Petri, A (Ed.), *Mechanics of earthquake faulting* (Vol. 202, pp. 81–94). doi: 10.3254/978-1-61499-979-9-81

McLaskey, G. C. (2019, dec). Earthquake Initiation From Laboratory Observations and Implications for Foreshocks. *Journal of Geophysical Research: Solid Earth*, *124*(12), 12882–12904. doi: 10.1029/2019JB018363

Mello, M., Bhat, H. S., & Rosakis, A. J. (2016, aug). Spatiotemporal properties of Sub-Rayleigh and supershear rupture velocity fields: Theory and experiments. *Journal of the Mechanics and Physics of Solids*, *93*, 153–181. doi: 10.1016/J.JMPS.2016.02.031

Morad, D., Sagy, A., Tal, Y., & Hatzor, Y. H. (2022, feb). Fault roughness controls sliding instability. *Earth and Planetary Science Letters*, *579*. doi: 10.1016/j.epsl.2022.117365

Nielsen, S., Taddeucci, J., & Vinciguerra, S. (2010, feb). Experimental observation of stick-slip instability fronts. *Geophysical Journal International*, *180*(2), 697–702. doi: 10.1111/j.1365-246X.2009.04444.x

Ohnaka, M., & Shen, L.-f. (1999). Scaling of the shear rupture process from nucleation to dynamic propagation: Implications of geometric irregularity of the rupturing surfaces. *Journal of Geophysical Research: Solid Earth*. Retrieved from https://agupubs.onlinelibrary.wiley.com/doi/abs/10.1029/1998JB900007 doi: 10.1029/1998jb900007

Palmer C., A., & Rice R., J. (1973). The Growth of Slip Surfaces in the Progressive Failure of Over-Consolidated Clay. *Proceedings of The Royal Society A: Mathematical, Physical and Engineering Sciences*, *332*(1591 DO - 10.1098/rspa.1973.0040), 527–548.

Passelègue, F. X., Almakari, M., Dublanchet, P., Barras, F., Fortin, J., & Violay, M. (2020, oct). Initial effective stress controls the nature of earthquakes. *Nature Communications 2020 11:1*, *11*(1), 1–8. Retrieved from https://www.nature.com/articles/s41467-020-18937-0 doi: 10.1038/s41467-020-18937-0

Passelègue, F. X., Schubnel, A., Nielsen, S., Bhat, H. S., & Madariaga, R. (2013). From sub-Rayleigh to supershear ruptures during stick-slip experiments on crustal rocks. *Science*, *340*(6137), 1208–1211. doi: 10.1126/SCIENCE.1235637

Pham-Ba, S., Brink, T., & Molinari, J.-F. (2020, apr). Adhesive wear and interaction of tangentially loaded micro-contacts. *INTERNATIONAL JOURNAL OF SOLIDS AND STRUCTURES*, *188*, 261–268. doi: 10.1016/j.ijsolstr.2019.10.023

Popov, V. L., Grzemba, B., Starcevic, J., & Fabry, C. (2010). Accelerated creep as a precursor of friction instability and earthquake prediction. *Phys. Mesomech.*, *13*(5-6), 283–291. doi: 10.1016/j.physme.2010.11.009

Rabinowicz, E. (1951). The nature of the static and kinetic coefficients of friction. *Journal of Applied Physics*, *22*(11), 1373-1379. Retrieved from https://doi.org/10.1063/1.1699869 doi: 10.1063/1.1699869

Read, B., Testing, J. D. P., & undefined 1981. (n.d.). Measurement of dynamic properties of polymeric glasses for different modes of deformation. *Elsevier*. Retrieved from https://www.sciencedirect.com/science/article/pii/

0142941881900313

Rice, J. R., Lapusta, N., & Ranjith, K. (2001, sep). Rate and state dependent friction and the stability of sliding between elastically deformable solids. *Journal of the Mechanics and Physics of Solids*, *49*(9), 1865–1898. doi: 10.1016/S0022-5096(01)00042-4

Ripperger, J., Ampuero, J. P., Mai, P. M., & Giardini, D. (2007, apr). Earthquake source characteristics from dynamic rupture with constrained stochastic fault stress. *Journal of Geophysical Research: Solid Earth*, *112*(4). doi: 10.1029/2006JB004515

Roch, T., Brener, E. A., Molinari, J.-F., & Bouchbinder, E. (2022, JAN). Velocity-driven frictional sliding: Coarsening and steady-state pulses. *JOURNAL OF THE MECHANICS AND PHYSICS OF SOLIDS*, *158*. doi: 10.1016/j.jmps.2021.104607

Rubino, V., Rosakis, A. J., & Lapusta, N. (2017, jun). Understanding dynamic friction through spontaneously evolving laboratory earthquakes. *Nature Communications*, *8*. doi: 10.1038/NCOMMS15991

Rubinstein, S. M., Cohen, G., & Fineberg, J. (2004). Detachment fronts and the onset of dynamic friction. *Nature*. doi: 10.1038/nature02830

Rubinstein, S. M., Cohen, G., & Fineberg, J. (2007, jun). Dynamics of precursors to frictional sliding. *Physical Review Letters*, *98*(22). doi: 10.1103/PHYSREVLETT.98.226103

Sagy, A., Brodsky, E. E., & Axen, G. J. (2007, mar). Evolution of fault-surface roughness with slip. *Geology*, *35*(3), 283–286. doi: 10.1130/G23235A.1

Sammis, C. G., & Rice, J. R. (2001). Repeating earthquakes as low-stress-drop events at a border between locked and creeping fault patches. *Bulletin of the Seismological Society of America*, *91*(3), 532–537.

Schär, S., Albertini, G., & Kammer, D. S. (2021, aug). Nucleation of frictional sliding by coalescence of microslip. *International Journal of Solids and Structures*, *225*. Retrieved from http://creativecommons.org/licenses/by/4.0/ doi: 10.1016/J.IJSOLSTR.2021.111059

Scholz, C. H. (2014). The Rupture Mode of the Shallow Large-Slip Surge of the Tohoku-Oki Earthquake. *Bulletin of the Seismological Society of America*, *104*(5), 2627–2631. doi: 10.1785/0120140130

Scholz, C. H. (2019). *The Mechanics of Earthquakes and Faulting*. doi: 10.1017/9781316681473

Schubnel, A., Nielsen, S., Taddeucci, J., Vinciguerra, S., & Rao, S. (2011, aug). Photo-acoustic study of subshear and supershear ruptures in the laboratory. *Earth and Planetary Science Letters*, *308*(3-4), 424–432. doi: 10.1016/j.epsl.2011.06.013

Schultz, R., Skoumal, R. J., Brudzinski, M. R., Eaton, D., Baptie, B., & Ellsworth, W. (2020). Hydraulic Fracturing-Induced Seismicity. *Reviews of Geophysics*, *58*(3), e2019RG000695. Retrieved from https://agupubs.onlinelibrary.wiley.com/doi/abs/10.1029/2019RG000695 doi: https://doi.org/10.1029/2019RG000695

Shlomai, H., Adda-Bedia, M., Arias, R. E., & Fineberg, J. (2020). Supershear Frictional Ruptures Along Bimaterial Interfaces. *Journal of Geophysical Research: Solid Earth*. doi: 10.1029/2020JB019829

Svetlizky, I., Bayart, E., Cohen, G., & Fineberg, J. (2017, jun). Frictional Resistance within the Wake of Frictional Rupture Fronts. *Physical Review Letters*, *118*(23). doi: 10.1103/PHYSREVLETT.118.234301

Svetlizky, I., & Fineberg, J. (2014). Classical shear cracks drive the onset of dry frictional motion. *Nature*, *509*(7499), 205–208. doi: 10.1038/nature13202

Svetlizky, I., Kammer, D. S., Bayart, E., Cohen, G., & Fineberg, J. (2017, mar). Brittle fracture theory predicts the equation of motion of frictional rupture fronts. *Physical Review Letters*, *118*(12). doi: 10.1103/

PHYSREVLETT.118.125501

Tabor, D. (1977). Surface forces and surface interactions. *Journal of Colloid and Interface Science*, *58*(1), 2–13. Retrieved from https://www.sciencedirect.com/science/article/pii/0021979777903666 doi: https://doi.org/10.1016/0021-9797(77)90366-6

Uchida, N., & Bürgmann, R. (2019). Repeating Earthquakes. *Annual Review of Earth and Planetary Sciences*, *47*(1), 305–332. Retrieved from https://doi.org/10.1146/annurev-earth-053018-060119 doi: 10.1146/annurev-earth-053018-060119

Uenishi, K., & Rice, J. R. (2003). Universal nucleation length for slip-weakening rupture instability under nonuniform fault loading. *Journal of Geophysical Research: Solid Earth*, *108*(B1). doi: 10.1029/2001JB001681

Wu, B. S., & McLaskey, G. C. (2019). Contained Laboratory Earthquakes Ranging From Slow to Fast. *Journal of Geophysical Research: Solid Earth*, *124*(10). doi: 10.1029/2019JB017865

Xia, K., Rosakis, A. J., & Kanamori, H. (2004). Laboratory Earthquakes: The Sub-Rayleigh-to-Supershear Rupture Transition. *Science*, *303*(5665). doi: 10.1126/science.1094022

Xu, S., Fukuyama, E., & Yamashita, F. (2019, jan). Robust Estimation of Rupture Properties at Propagating Front of Laboratory Earthquakes. *Journal of Geophysical Research: Solid Earth*, *124*(1), 766–787. doi: 10.1029/2018JB016797

Xu, S., Fukuyama, E., Yamashita, F., Mizoguchi, K., Takizawa, S., & Kawakata, H. (2018, may). Strain rate effect on fault slip and rupture evolution: Insight from meter-scale rock friction experiments. *Tectonophysics*, *733*, 209–231. doi: 10.1016/j.tecto.2017.11.039

Yamashita, F., Fukuyama, E., Xu, S., Mizoguchi, K., Kawakata, H., & Takizawa, S. (2018, may). Rupture preparation process controlled by surface roughness on meter-scale laboratory fault. *Tectonophysics*, *733*, 193–208. doi: 10.1016/J.TECTO.2018.01.034